Physics – Uspekhi **57** (10) 945 – 958 (2014)

REVIEWS OF TOPICAL PROBLEMS

PACS numbers: **61.46. – w**, 61.82.Rx, 62.20.F – , **65.80. – g**, 81.65.Kn

Nanostructures under extremes

R A Andrievski

DOI: 10.3367/UFNe.0184.201410a.1017

Contents

Abstract. This paper reviews current research into the behavior of nanostructures under extreme conditions such as high temperatures, irradiation, and deformation. It describes methods for enhancing the stability of nanostructures under these conditions and identifies aspects that have not yet been given sufficient attention.

1. Introduction

The behavior of materials and compounds under extreme conditions is currently attracting increasingly greater interest (see [1–6]). This issue was discussed at several recent symposia in the USA and Europe held by The American Ceramic Society (2012), The Minerals, Metals & Materials Society (2013), The Materials Research Society (2013, 2014), The European Materials Research Society (2014), at the International Conference on Modern Materials and Technologies (2014), the Materials Science and Engineering Congress (2014), and others. Substances and materials are investigated under different extreme conditions to extend the scope of information needed for a deeper understanding of fundamental problems in the physics and chemistry of high energy densities, astrophysics, and geology, not to mention numerous applications in connection with special requirements and operating conditions for present-day and future technical devices, medical instruments, and biological objects.

These considerations account for the ongoing tendencies in the development of nanostructured materials extensively being discussed in the current literature (see [6–10]).

R A Andrievski Institute of Problems of Chemical Physics, Russian Academy of Sciences, prosp. Akademika Semenova 1, 142432 Chernogolovka, Moscow region, Russian Federation
Tel. +7 (496) 522 77 93. Fax +7 (496) 522 35 07
E-mail: ara@icp.ac.ru

Received 9 January 2014, revised 23 February 2014
Uspekhi Fizicheskikh Nauk **184** (10) 1017 – 1032 (2014)
DOI: 10.3367/UFNr.0184.201410a.1017
Translated by Yu V Morozov; edited by Z P Svitan'ko

The specific behavior of nanostructures is due in the first place to the fact that most of them (excluding supramolecular systems) are essentially nonequilibrium. A variety of interfaces in the form of grain and phase boundaries, triple and quadruple junctions, and residual stresses and defects, segregations, and nonequilibrium phases, on the one hand, stimulate manifestations of high-level physicomechanical properties of nanomaterials (compared with ordinary macrocrystalline objects). On the other hand, the excess free energy in nanostructures imposes strict requirements on their stability. Evidently, high temperatures, deformation, corrosion, and irradiation may induce recrystallization, segregation, homogenization, relaxation, phase transition, phase formation and degradation, amorphization, sintering, and the filling of micro- and nanopores (nanocapillaries). Taken together, these processes are responsible for the evolution and sometimes annihilation of a nanostructure leading to alteration (deterioration) of its physical, mechanical, chemical, and biological properties. Therefore, elucidation of consistent stability patterns of nanostructures is of special importance as one of the key problems in modern nanomaterials science. We discussed selected aspects of this problem in earlier publications [7, 10–15], but the rapidly growing body of new data in this field requires a more comprehensive analysis and generalization of various aspects of the thermal, radiation, and strain resistance of nanostructures, taking account of their dimensional characteristics. The present review is designed to consider these issues.

2. Thermal stability

2.1 Theoretical approaches and modeling

Heating nanomaterials results in grain growth and Gibbs free energy reduction (ΔG due to contraction of the grain boundary area. Grains in nanomaterials grow by migration and fusion or rotation and fusion (Fig. 1). The mechanism of rotation is much less known, even though a few recent publications report new data on the peculiarities this process in nanomaterials. It was shown by molecular dynamics (MD) methods that the two mechanisms may

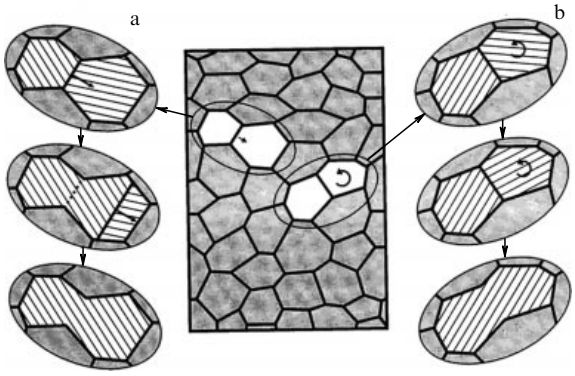

Figure 1. Schematic of grain growth mechanism: the initial state (in the middle); (a) migration and fusion, (b) rotation and fusion (adapted from [16]).

simultaneously operate in nanostructures, with the rate of rotation and the size of its fraction relative to that of migration increasing with decreasing grain size [17]. Ref. [18] demonstrated the dependence of the rotation rate on the coupling geometry of adjoining grains. The formation of low-energy small-angle boundaries during rotation as exemplified by 20- and 200-nm yttrium oxide grains was observed in a temperature range of 600–1000 °C [19]. An interesting example of collective grain rotation of nanocrystalline Ti, TiN, and NiO layers under irradiation with high-energy gold ions ($E = 350$ MeV) taking account of pole figures is reported in [20].

The growth of grains in consolidated nanomaterials can be hampered (to prevent degradation of the nanostructure) by the following methods: retardation by second-phase particles and pores, alteration of the initial grain size, decrease in grain mobility by doping (including the creation of segregations at grain boundaries), and high-temperature spinodal decay. The curvature-driven boundary migration rate is usually written in the form

$$v = MP = M_0 \exp\left(\frac{-Q_\mathrm{m}}{RT}\right)\frac{2\gamma_\mathrm{g}}{r_\mathrm{g}}\,, \qquad (1)$$

where M is the mobility, M_0 is the pre-exponential factor, P is the driving force, Q_m is the boundary migration activation energy, γ_g is the grain boundary energy, and r_g is the grain radius curvature. There are two generally accepted approaches to the description of grain growth inhibition: the kinetic approach takes account of reduced mobility M while the thermodynamic one is focused on a decrease in the driving force P due to low grain boundary energy γ_g. The theoretical bases of these approaches are different, but inhibition of the grain growth has been long and extensively used in practical applications of materials science. Grain growth inhibition by nanoinclusions (the so-called Zener pinning mechanism) is described by the following expression:

$$P_\mathrm{Z} = \frac{3V_r\gamma_\mathrm{i}}{2r}\,, \qquad (2)$$

where P_Z is the Zener drag pressure on the unit boundary area, V_r is the volume fraction of nanoinclusions with radius r, and γ_i is the interfacial surface energy of these inclusions. It follows from (2) that effective retardation of grain growth can be achieved by increasing the number of nanoinclusions and decreasing their radius.

Numerical simulation of possible nanoinclusion movements during the migration of grain boundaries revealed a dualism in nanostructure evolution, namely that the presence of nanoparticles, depending on their volume fraction and overall migration rate of the boundaries, can not only decrease, but also increase their mobility and thereby promote anomalous growth [21, 22]. The analysis of different scenarios of grain–pore interplay has shown that the growth of the former and the disappearance of the latter during annealing obey different kinetic strategies, depending on component size and mobility [23].

Of special importance in the investigation of grain boundary motion in the framework of the thermodynamic approach are studies on the development of the thermodynamics of two-component nanosystems with the use of methods allowing the free Gibbs energy ΔG for alloys to be determined taking into account not only the concentration factor but also the presence of nanograins [24–27]. The key issue in these investigations is the application of the usual regular solution approximation for both intergrain (segregation) spaces and grain internal spaces. Omitting intermediate calculations, the final expression for the total ΔG value can be written as [25, 26]

$$\Delta G = (1-f_\mathrm{b})\,\Delta G_\mathrm{g} + f_\mathrm{b}\Delta G_\mathrm{b} + z\psi f_\mathrm{b}(X_\mathrm{b} - X_\mathrm{g}) \times \left[(2X_\mathrm{b}-1)\,\omega_\mathrm{b} - (zt)^{-1}(\Omega^B\gamma_\mathrm{g}^B - \Omega^A\gamma_\mathrm{g}^A)\right]. \qquad (3)$$

Here, ΔG_g and ΔG_b are the free Gibbs energies for grain internal spaces and intergrain spaces, respectively, f_b is the volume fraction of intergrain spaces equaling $1-[(d-t)/d]^3$, d is the grain size, t is the intergrain space width, usually assumed to equal 0.5–1 nm, z is the bulk coordination number, ψ is the fraction of atoms with interatomic bonds in intergrain spaces, X_b and X_g are the concentrations in intergrain spaces and grain internal spaces satisfying the relation for the mean concentration $X = f_\mathrm{b}X_\mathrm{b} + (1-f_\mathrm{b})\,X_\mathrm{g}$, Ω^A and Ω^B are the atomic volumes of alloy components $A + B$ (addition), γ_g^A and γ_g^B are their grain boundary specific energies, and ω_b is the interaction parameter in an intergrain space defined in the regular solution theory through the pair interaction energy E

$$\omega = E^{AB} - \frac{E^{AA} + E^{BB}}{2}\,.$$

The use of expression (3) and variations of d values and thermodynamic properties permits computing ΔG surfaces and finding from their minimums the characteristics for the thermally most stable nanoalloys. By way of example, Fig. 2 shows the dependence of ΔG on the grain size and concentration in the intergrain space. It is clear that at given values of total concentration X, temperature T, and interaction parameter ω_b, the minimum ΔG value corresponds to an alloy with a grain size around 25 nm and practically complete segregation of one of the components at the grain boundaries.

Ref. [26] presents a detailed analysis of various cases of ΔG minimization with regard to the grain size and phase decay (variations of composition, temperature, and interaction parameters, the absence of a ΔG minimum, various combinations of mixing and segregation enthalpies, the formation of amorphous interlayers in intergrain spaces, the presence of metastable nanoalloys, the formation of two-component nanocomposites, etc.).

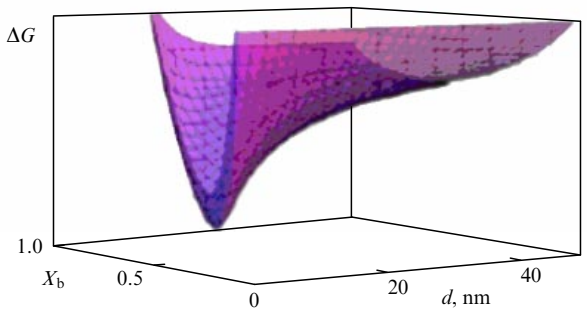

Figure 2. Variations of the free Gibbs energy ΔG depending on grain size d and concentration in the intergrain space X_b (adapted from [26]).

Figure 3 demonstrates the dependence of segregation enthalpy ΔH^{segr} on the enthalpy of mixing ΔH^{mix} for different tungsten-based alloys ($T = 1100\,^{\circ}C$) [25]. The enthalpy values were calculated from the following formulas:

$$H^{segr} = z\left(\omega_g - 0.5\omega_b - \frac{\Omega^B\gamma_g^B - \Omega^A\gamma_g^A}{2zt}\right),$$

$$\Delta H^{mix} = z\omega_g X(1-X).$$

The nanocrystalline state is inherent in the alloys that are shown above the dependence $\Delta H^{segr} = f(\Delta H^{mix})$, while the coarse-grained ones lie in region (*2*) under the curve.

The same approach based on the regular solution approximation for intra- and intrergrain regions [24] was developed in Ref. [27], where the influence of temperature on the size of nanograins and segregations in intergrain spaces was calculated for Fe–Zr, Cu–Zr, Cu–Nb, and Ni–W alloys with varying concentrations of the second component. The authors of [27] calculating ΔG took into consideration the contribution of elastic interaction, besides the purely chemical one, to alloy formation and assumed the grain boundary energy to be 1/3 of the surface energy. Analysis of the computed results showed that a decrease in grain growth during the annealing of nanoalloys is especially pronounced for small additions of zirconium to iron.

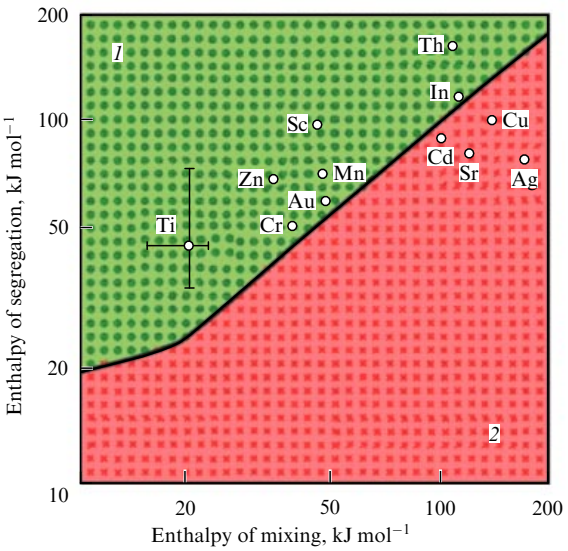

Figure 3. Stability of tungsten-based alloys at 1100 °C: *1* — region of nanocrystalline alloys, *2* — region of coarse-grained alloys (adapted from [25]).

The evaluation of a possible decrease in the grain boundary energy taking into account the contribution of chemical and elastic interactions was further considered in Ref. [28], where concentrations of additions necessary to ensure thermal stability in two-component nanoalloys (grain size of 25 nm, homologous temperature of $0.6T_m$ with respect to the metal solvent, where T_m is the melting temperature) was calculated for more than 1000 binary metallic systems.

Another method for taking account of the thermodynamic properties of intergrain spaces and grain internal spaces was proposed in [29, 30] with reference to the difference in the free volume ΔV for grain boundaries and bulk crystal. The total values of enthalpy (H), entropy (S), and free energies are written from additive considerations as

$$H = X_b H_b(\Delta V, T) + (1 - X_b)\, H_g(T)\,, \tag{4}$$

$$S = X_b S_b(\Delta V, T) + (1 - X_b)\, S_g(T)\,, \tag{5}$$

$$G = X_b G_b(\Delta V, T) + (1 - X_b)\, G_g(T)\,, \tag{6}$$

where $\Delta V = (V_b/V_g) - 1$, and V_b and V_g are unit cell volumes in intergrain spaces and grain internal spaces, respectively. Such a form for ΔV implies an excess volume due to a disordered arrangement of atoms at the grain boundaries ($V_b > V_g$). The values of ΔV and thermodynamic functions for intergrain spaces, including those of thermal capacity and Debye temperature, are accepted with due regard for the available experimental data (see [31]). This method was used to estimate temperature stability and phase transformations in an Sm–Co system ($SmCo_5$, Sm_2Co_{17}, $SmCo_7$, etc.) [29, 30, 32, 33]. A computation of temperature and grain size-dependent thermodynamic functions of $SmCo_7$ showed that all of them increase at constant temperature as the grain size decreases, especially when d becomes smaller than 40 nm [30].

Other theoretical studies worthy of note include evaluation of spinodal decay conditions in $Al_2O_3-ZrO_2$ and TiN–SiN quasi-binary systems and interface behavior in type TiN/SiN/TiN and other multilayer nanocomposites [34–39]. Refs [34–36] are remarkable for the combination of methods based on the thermodynamic approach and calculations in the approximation of the density functional theory. It creates an opportunity to determine not only thermodynamic characteristics (ΔG, ΔH, etc.) but also parameters of electronic and crystal structure and elastic moduli. Calculations showed that the top of the spinodal and binodal decay dome of a metastable $TiN^{GCK}-SiN^{GCK}$ system lies at the level of ~ 3200 K and the system is practically two-phase at $T < 1273$ K [34].

The use of the first-principle MD method made it possible to elucidate the characteristic features of interface thermal stability in various heterostructures of TiN/SiN and TiN/Si_3N_4 monolayers in a temperature range of 0–1400 K [37, 38]. The same method was employed in [39] to compare the thermal behavior of titanium nitride-based monolayer heterostructures with those of various nitrides and carbides. The analysis of evolution of atomic configurations near the interfaces between cubic modifications of TiN (001) and BN, AlN, SiC, or SiN showed that the monolayer TiN/AlN heterostructure is the most stable of them in a temperature range from 0 to 1400 K. The same conclusion was made based

on density variations of phonon and electron states for all heterostructures being analyzed. It was noted that the thermal instability of cubic SiN may be related to vacancy formation in the silicon sublattice [37]. The role of dimensional effects and the influence of diffusive mixing (inevitable during long-time high-temperature exposure) were not considered in [34–39] in the framework of theory constraints.

2.2 Experimental results

The thermal stability of copper, iron, and nickel nanocrystalline alloys is the most thoroughly studied. Figure 4 illustrates the temperature dependence of grain growth in Cu–Zr, Fe–Zr, Fe–Ni, Fe–Ta, and Fe–Cr systems [40, 41]. It shows that doping increases thermal stability, with zirconium and tantalum having an especially strong influence on this parameter. Theoretical and experimental findings for a Cu–5 at.% Zr alloy in a temperature range of 300–700 °C (see Fig. 4) are presented in Table 1 showing the 4–10-fold difference between theory and experiment. This result may be considered satisfactory, taking into account the approximate nature of the model [27].

The nanocrystalline state of the W–Ti alloy (Fig. 3) predicted in [25] was confirmed in experiments using a W–20 at.% Ti powder with a starting nanograin size of 20 nm that remained virtually unaltered after annealing at 1100 °C for one week. The grain size of undoped tungsten under the same conditions was 600 nm [25]. The study of Ti distribution in a nanostructure revealed its nonuniform character with variations from 0 to 50 at.%; this means that the thermal stability of a W–20 at.% Ti alloy under these conditions could be due not only to a decrease in the free energy but also to the appearance of segregation inclusions and Zener pinning. A similar situation (i.e., the action of two mechanisms) could take place in annealing of Cu–5 at.% Zn alloys at 700 °C when the difference between the theory (taking account of a single mechanism) and experiment reached a maximum (see Table 1).

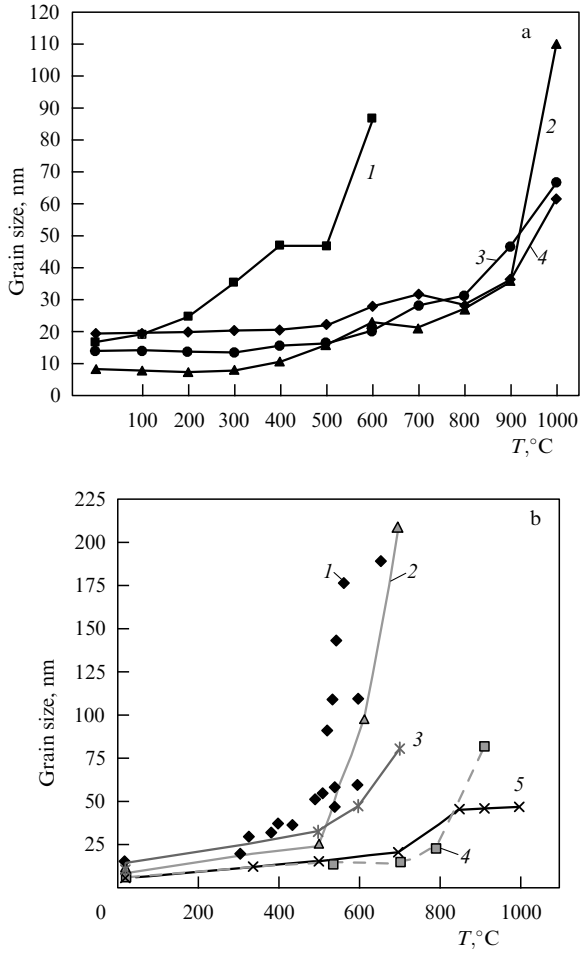

Figure 4. Effect of temperature on the grain size during 1 hour of annealing of (a) copper alloys (*1* — pure copper; *2* — Cu – 5 at.% Zr; *3* — Cu – 2 at.% Zr; *4* — Cu – 1 at.% Zr) and (b) iron alloys (*1* — pure iron, *2* — Fe – 1 at.% Ni; *3* — Fe – 10 at.% Cr; *4* — Fe – 1 at.% Ta; *5* — Fe – 1 at.% Zr) (adapted from [40, 41]).

Table 1. Theoretical and experimental grain size in an annealed Cu–5 at.% Zr alloy.

Source	Grain size (nm) after annealing at °C		
	300	500	700
Theory [27]	35	55	220
Experiment [41]	9	15	22

Koch and co-workers [42] compared the effectiveness of kinetic and thermodynamic approaches for hampering the thermal growth of nanograins based on experimental results obtained by different authors. On the one hand, they normalized these data to melting temperature (T_m) at the homologous temperature scale and, on the other hand, took into account only grains smaller than 100 nm in annealed samples measured by transmission electron microscopy (TEM) and X-ray diffraction analysis (XRD). Alloys based on Al, Mg, Cu, and Fe with Al_2O_3, AlN, ZrO_2, and Nb nanoinclusions proved thermally stable at high temperatures up to $(0.75-0.85)\,T_m$, whereas alloys based on Ni, Co, Fe, Y, RuAl, and TiO_2 with W, P, Zr, Fe, and Ca admixtures were less stable, namely, up to $(0.35-0.65)\,T_m$.

Copper-based alloys doped with W and Ta (10 at.%) showed high thermal stability [43, 44]. They were prepared by high-energy cryogenic grinding ($T = -196$ °C) of the starting powders, followed by pressure sintering. The initial grain size in Cu–W alloys was ~ 15 nm and increased to $d \sim 60$ nm after annealing at 800 °C [43]. Cu–Ta alloys were investigated more thoroughly. The results are presented in Table 2, showing the rather high thermal stability of these materials. To compare, the microhardness of Cu–10 at.% W alloys before and after annealing at 800 °C was 3 and 2.6 GPa, respectively [43], i.e., lower than in [44] (see Table 2). The detailed discussion of the data obtained and different thermal stability mechanisms associated with the influence of triple junctions, doping, inclusions, and segregation enabled the authors of [44] to conclude that the high thermal stability of Cu–Ta alloys is due to the formation and subsequent decay of

Table 2. Changes in nanostructure and microhardness of Cu–10 at.% Ta alloys after annealing in an atmosphere of hydrogen for 4 hr (adapted from [44]).

Annealing temperature (homologous temperature), °C	Nanograin size, nm		Microhardness, GPa
	Cu	Ta	
20 ($0.22T_m$) — initial state	6.7	6	4.8
540 ($0.6T_m$)	21 ± 4	22 ± 5	~ 3.6
770 ($0.77T_m$)	54 ± 9	37 ± 9	ND
900 ($0.87T_m$)	111 ± 26	42.5 ± 25	3.4
1040 ($0.97T_m$)	167 ± 50	99 ± 99	2.6

tantalum segregations at grain boundaries, i.e., the joint action of thermodynamic and kinetic mechanisms. The latter mechanism begins to operate at high temperatures as a result of the breakdown of boundary layers into inclusions (nanoclusters according to the terminology in [44]). This inference is confirmed by MD calculations and experimental studies using TEM [45].

The important role of the kinetic mechanism in thermal stability due to inhibition by nanoprecipitates was demonstrated for Cu–Nb, Ni–Y, and Fe–Zr nanoalloys [46–48], in contrast to Cu–Fe and Pd–Zr alloys [46, 47].

Generally speaking, however, mechanisms of layer breakdown and nanoinclusion formation are still poorly known, and the search for new thermally stable nanomaterials is based on the concepts of traditional materials science concerning the creation of dispersion strengthened objects with the use of various technological tools. For example, new grades of ferrite and ferrite–martensite nanosteels are fabricated by powder technology (high-energy milling of starting components and consolidation without the loss of nanostructure) [12, 49]. The presence of 2–4 nm type $Y_2Ti_2O_7$ and Y_2TiO_5 oxide inclusions characterized by thermodynamic stability and good matrix adhesion in these iron–chromium steels creates a prerequisite for high thermal resistance of the nanostructure and, accordingly, high mechanical properties under conditions of radiation exposure (see Section 3).

Worthy of note are the results obtained with the use of multilayer nanofilms [50–54]. The high strength and plasticity of copper films with twin intermediate nanolayers have been known for a long time [11, 55], but studies of annealing effects also revealed the high thermal stability of these structures [50, 54]. This follows from Fig. 5, with the inset showing the enlarged graph that the width of the twin interlayers (nanolamellae), responsible for high hardness, changes but insignificantly, unlike the growth of main nanograins. The high hardness persists even after annealing at 800 °C ($0.74T_m$), which is much higher than for ordinary nanocrystalline copper but lower than for a Cu–Ta alloy (Table 2). Refs [50, 54] demonstrated the low temperature sensitivity of low-angle coherent interlamellar boundaries in Cu and Ni in comparison with high-angle boundaries typical of conventional nanomaterials.

Type Cu/Nb bulk two-phase nanocomposites with a layer thickness up to 5–10 nm fabricated by the multi-pack rolling technique are also characterized by high strength and thermal stability [51–53]. For example, nanolaminates with a $\{551\}\langle 1110\rangle Cu||\{112\}\langle 111\rangle Nb$ interface underwent deformation twinning, while the hardness of these two samples after annealing at 500 °C decreased by less than 1.5% (from 4.13 to 4.06 GPa), i.e., this parameter was higher than all known values for such nanocomposites [53].

The above examples of thermal stability mostly included consolidated metallic nanomaterials finding extensive application in high-temperature technologies. This issue is equally important for isolated micro- and nanoparticles used in such fields as photoelectric transformation, heterogeneous catalysis, and the sensor technique. For example, photonic tungsten microcrystals obtained by atomic layer deposition into a self-organizing SiO_2 template matrix retain their optic properties upon heating up to 1400 °C; also, photonic hafnium diboride HfB_2 microcrystals have promising applications [56]. Various methods for stabilizing the sizes and properties of gold and copper nanoparticles (e.g., prevention of sintering) are

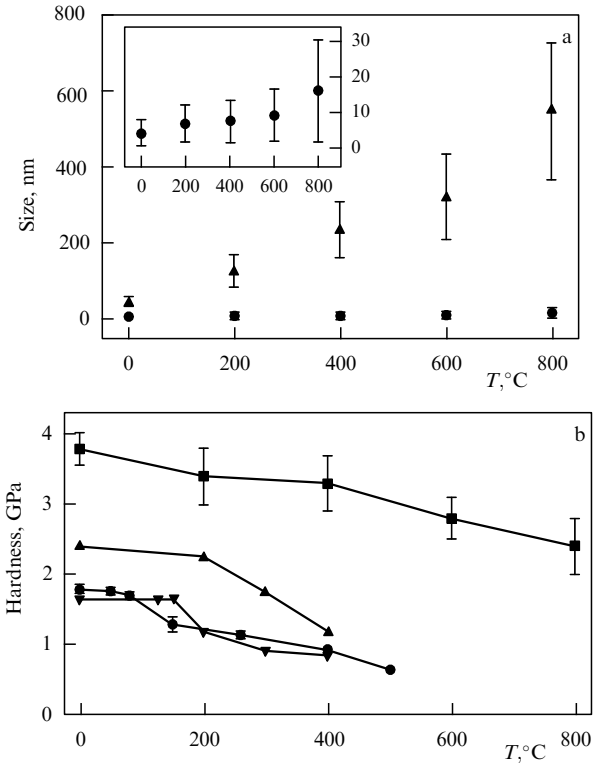

Figure 5. Effect of annealing temperature on the grain growth and twin interlayer width (a) and on the hardness (b) of copper samples with different structures: (a) ▲ is the grain size, ● is the twin interlayer width, (b) ■ is films with the nanotwin structure, ▲ ● ▼ are ordinary samples with the ultrafine-grained and nanocrystalline structure (data from different authors; adapted from [50]).

discussed in [57, 58]. Particular examples of grain growth in Al, Zr, Ti, and Sn nanooxides can be found in [59, 60], while the role of triple junctions in the retardation of Y_2O_3 grain growth is analyzed in [61].

2.3 Anomalous grain growth

Anomalous grain growth (or secondary recrystallization) leading to the appearance of large grain aggregates absorbing smaller neighbors in macrocrystalline materials has been known and investigated for a long time [62]. The same phenomenon in nanomaterials observed not only during heating but also at room temperature results in complete or partial annihilation of the nanostructure and the appreciable loss of properties; this accounts for the importance of studying anomalous grain growth and developing methods for its prediction and prevention. Given normal growth, the grains retain their log-normal distribution, whereas large-grain clusters appear in an anomalous situation [63], and the structure becomes bimodal (see data on the rise in mean square measurement error with temperature in Table 2).

Figure 6 shows experimental [64] and theoretical [65] data on grain growth kinetics in nanocrystalline palladium at room temperature. Evidently, the two sets of data are in good agreement till the onset of anomalous growth (over 8 hr in duration). At the same time, the discrepancy between them is well apparent if inhibition by triple and quadrupole junctions is disregarded. Nevertheless, neither the large number of junctions nor residual porosity (initial grain size ~ 5 nm, sample porosity 4%) and impurities (0.4 at.% H, 0.2 at.% N, 0.1 at.% O) prevented anomalous growth that

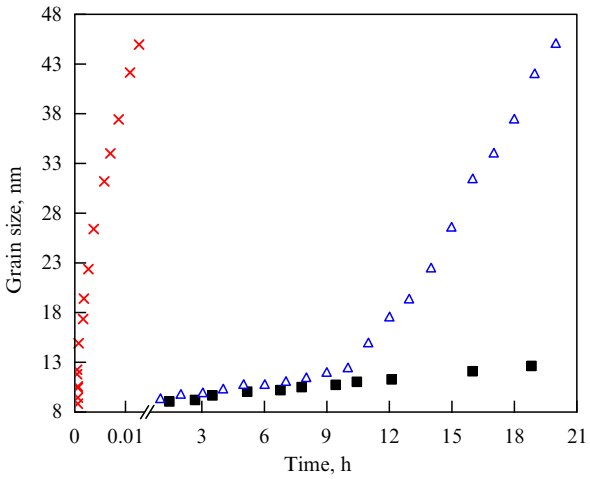

Figure 6. Grain growth kinetics in nanocrystalline palladium at room temperature: △ is experiment [64], ■ and × are the calculated results [65] (adapted from [65]).

turned the palladium nanostructure into an ordinary microstructure with a grain size of ~ 10 μm after exposure to room temperature for about 2 months [64].

The anomalous grain growth at room and higher temperatures was observed in experiments with many other nanomaterials based on copper [44, 66], nickel [63, 6, 68], iron [69, 70], WC–Co [71], and diamond [72] (see also references to earlier studies in [11, 71], including those with the use of *in situ* TEM methods [44, 67–69]). It should be emphasized that the above nanomaterials were fabricated by such different methods as pulsed electrodeposition [63], compression and sintering [64, 72], intensive plastic deformation (torsion under 4.5 GPa pressure at liquid nitrogen temperature) [66], pulsed laser deposition [67, 68], intense mechanical grinding + mixing (mechanosynthesis) [44, 69, 70], and high-pressure sintering ($T = 1400\,^{\circ}\mathrm{C}$, $P = 6.8$ GPa) [73]. Naturally, such a variety of methods has given different types of data on both the starting and the final states of the study objects. For example, *in situ* electron microscopy of annealed Ni films [67, 68] revealed numerous tetrahedral packing defects and dislocation loops, along with the formation of low-energy twin boundaries. The instability of the Cu nanostructure at room temperature brought the authors of [66] to the conclusion that low-temperature plastic deformation has no prospects to serve as a method for manufacturing nanomaterials. *In situ* studies of $Fe_{91}Ni_8Zr_1$ thermal stability showed that the anomalous grain growth begins above 700 °C in connection with the formation of γ-phase crystals having the facet-centered cubic (fcc) structure [70].

A theoretical description of anomalous grain growth in nanomaterials was proposed by V Yu Novikov [21, 22, 74–77]. Using an earlier model of temperature-related evolution of grain structure, the kinetic dependences of grain growth were written taking account of the differences in mobility, and the number and size of nanoinclusions slowing the growth. Numerical simulation showed an increasing tendency toward anomalous growth with greater mobility of nanoinclusions, while the influence of their number and radius is nonmonotonic. Moreover, it turned out that the number of nanoinclusions and pores needed to hamper grain growth is inversely proportional to the initial size of the nanograins.

For all that, reliable methods for the prediction and prevention of catastrophic enlargement of nanostructures analogous to that in Fig. 6 are still absent, and many important aspects of anomalous grain growth in nanomaterials (influence of defects and admixtures, relationship between thermodynamic and kinetic factors, choice of technology, etc.) await further detailed investigation.

3. Radiation stability

3.1. General characteristic. Modeling and microscopic approaches

Information on the behavior of nanomaterials on exposure to radiation is very important for designing fusion–fission reactors of the new generation (fast neutron reactors, high-temperature gas-cooled reactors, thermonuclear reactors, etc.). Materials used in these units must withstand long-term exploitation in strong radiation fields and corrosive environments at high temperatures and under severe stress. Naturally, new materials for nuclear and thermonuclear power engineering must by very stable.

The simplest picture of radiation defects arising in ordinary metals implies that bombardment with high-energy particles and neutrons leads to partial transfer of their energy to displaced atoms of the crystal lattice and the appearance of primary knock-on atoms (PKAs). These are the so-called displacement cascades consisting of Frenkel pairs in the form of interstitial atoms and vacancies (IAVs) and their complexes (clusters) in the form of loops and vacancy nanopores. Interaction between point radiation defects may cause their annihilation and removal along interfaces functioning in this case as sinks. The main aftereffects of radiation treatment include amorphization, reduced ductility (radiation hardening), and embrittlement (with a possible increase in the creep rate at high temperatures) due to the elevated defect content, swelling (volume expansion) owing to noncompensated vacancy sinks, and transmutation as a result of nuclear reactions or radioactive decay. The nature of the radiation process in nanoobjects is less known than that in usual macrocrystalline materials [78], and research on radiation defects in nanostructures is still in its infancy [12, 79, 80].

At least three scenarios of nanomaterial behavior under irradiation are conceivable from general considerations and the available experimental data:

(1) A large number of interfaces (grain boundaries and triple junctions) functioning as sinks for radiation defects promotes stabilization of nanomaterials compared with usual coarse-grained materials.

(2) Radiation defects promote nanostructure annihilation and transformation into an amorphous state.

(3) Irradiation may cause recrystallization and segregation affecting the realization of the two former scenarios.

Molecular dynamics methods (see [81–100]), including multiscale ones, are widely used to describe nanomaterials exposed to radiation. The following situations resulting from the bombardment of nanostructures with high-energy ions and neutrons have been simulated: displacement cascades in Ni nanograins ($d = 5$ and 12 nm) for particles with bombardment energies of 5, 20, and 30 keV [81], radiation-stimulated grain growth in nano-Ni ($d = 5$ and 10 nm) for a cascade excited by particle impact with an energy of 5 keV [82], interstitial atom and tetrahedral packing defect behavior in damage cascades [83], the evolution of nanocrystalline film morphology in response to irradiation [84, 85], the behavior

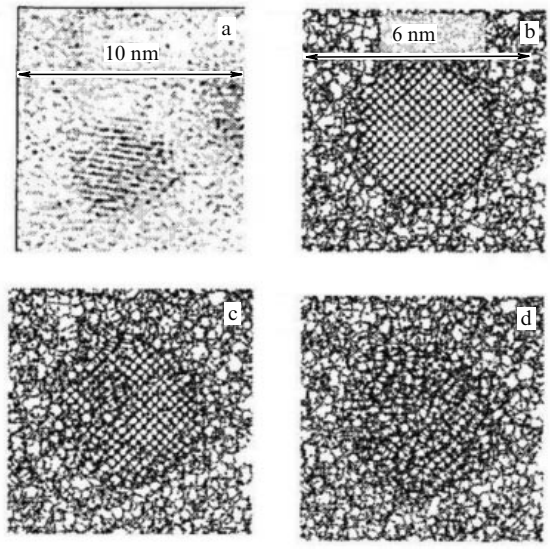

Figure 7. High-resolution TEM image of a Ge nanocrystal in an amorphous SiO_2 matrix (a) and model images of Ge/SiO_2 before (b) and after (c) irradiation at 1.7 eV per atom or 4 eV per atom (d) (adapted from [91, 93]).

of nanomaterials with a body-centered cubic (bcc) and fcc structure [86] under irradiation, behavior of point defects in nanostructures [87], nucleation and growth of vacancy clusters in the cubic modification of silicon carbide [88], grain boundary behavior in nanostructures functioning as sinks and sources of defects [89], the development of cascades in grain structures [90], amorphization of irradiated nanocrystals in amorphous matrices [91–93], absorption and emission of introduced atoms and vacancies by grain boundaries [94, 95], the behavior of silicon carbide, boron nitride, titanium oxide, and graphene exposed to radiation [88, 96–100], and others. These studies have demonstrated the important role of grain boundaries and triple junctions as sinks for radiation defects, the nature of radiation-stimulated grain growth, changes in surface roughness, and the stressed state in films. Moreover, they showed that vacancy clusters in irradiated bcc and fcc structures predominate in the looser bcc crystal lattices. Figure 7 presents a high-resolution TEM image of a germanium nanocrystal in an amorphous SiO_2 matrix and model images of a Ge/SiO_2 system calculated by the MD method before and after irradiation that illustrate progressive amorphization [91, 93].

Let us consider in more detail certain results of cascade modeling in vanadium [90] and copper [94]. Crystallites in the vanadium bcc contained $\Sigma 13\,\langle 320\rangle[001]$ and $\Sigma 17\,\langle 410\rangle[001]$ symmetric tilt boundaries, with the number of atoms per calculated cell varying from 6500 to 450,000 (depending on the PKA energy from < 0.5 to > 0.5 keV); $T = 10$ K [90]. The evolution of cascades was considered with regard to the duration of three stages, viz. ballistic (distribution of energy transferred to PKA over the entire volume of the model object with the maximum number of defects and appearance of thermal peaks), recombination (reduction in the number of defects to a certain constant value), and diffusion (further decrease in the number of defects limited by their interaction and transport). The results of modeling indicate that extended interfaces affect the formation of displacement cascades, because they accumulate a large fraction of radiation defects and prevent cascade propagation; sometimes (depending on the PKA energy) they become an impenetrable barrier for the cascades.

Modeling the interaction of IAV Frenkel pairs with grain boundaries in fcc copper allowed proposing the following mechanism behind recombination of these defects: first, the boundaries are saturated with highly mobile interstitial atoms, then these atoms are re-emitted and absorbed by vacancies in boundary regions [94]. By representing interfaces as special $\Sigma 11\,\langle 110\rangle\{131\}$ symmetric tilt boundaries and by modeling the situation for 15 cascades in copper (PKA kinetic energy 4 keV, total number of atoms in the system around 160,000, number of atoms in motion $\sim 130,000$), it was possible to estimate the influence of temperature on the time of removal of vacancies and interstitial atoms along the grain boundaries and in the case of their re-emission. Calculations showed that this process in a temperature range of 10–15 K is rather long ($t > 10^{10}$ s), and none of the mechanisms operate. At 70–100 K ($t < 1$ s), the main role is played by interstitial atoms, and all mechanisms operate at $T = 300$ K. A similar approach was used to estimate radiation damage in TiO_2 at 300 and 1000 K [99]. The complicated character of interface-defect interactions suggests that a decrease in the grain size in rutile TiO_2 increases radiation stability at high temperatures and lowers it at 300 K.

Ref. [94] helps to explain the results of experiments on variation of electrical resistance in Au foils measuring $(0.5 \times 10 \times 5.3) \times 10^{-3}$ mm (width, length, height) irradiated at 15 and 30 K (Fig. 8) [101]. The increment of electrical resistance suggests that nanosamples ($d \sim 23$ nm) were more prone to radiation damage at low temperatures [when none of the radiation defect removal mechanisms operated (see [91])] than their macrocrystalline analogs. On the contrary, the nanostructures exhibited higher radiation stability at room temperature when all three mechanisms operated.

Modeling competition between radiation defect absorption by grain boundaries and their volume recombination showed that cascadeless irradiation of copper with electrons increases the accumulation of vacancies from IAV Frenkel pairs on the boundaries at short times as the grain size decreases within a 40–15 nm range, but thereafter absorption by large grains begins to prevail [95].

Microscopic approaches to the assessment of the influence of irradiation on nanostructures were developed in [102–105]. The authors considered the formation of IAV Frenkel pairs in high- and low-energy interactions. In the former case, IAVs arose both at nanograin boundaries and inside the grains, whereas in the second case vacancies occurred only at the boundaries and interstitial atoms formed inside the grains [102]. The evolution of the defect behavior was analyzed for the following stages: (1) radiation-induced generation of defects, (2) absorption of defects by grain boundaries, (3) IAV annihilation, (4) formation of stable clusters of point defects. Processes (1) and (2) were assumed to prevail in high-energy impacts. A pre-eminent amorphization region was distinguished based on energy considerations with due regard for nanograin size. On the one hand, the well-developed interface (grain boundary) network contributes to a rise in the excess free energy and lowers the energy barrier for amorphization; on the other hand, it promotes removal of radiation defects and prevents amorphization.

An energy-based approach was developed in [103], where a qualitative picture was presented for free energy changes depending on grain size, and the conclusion was drawn that

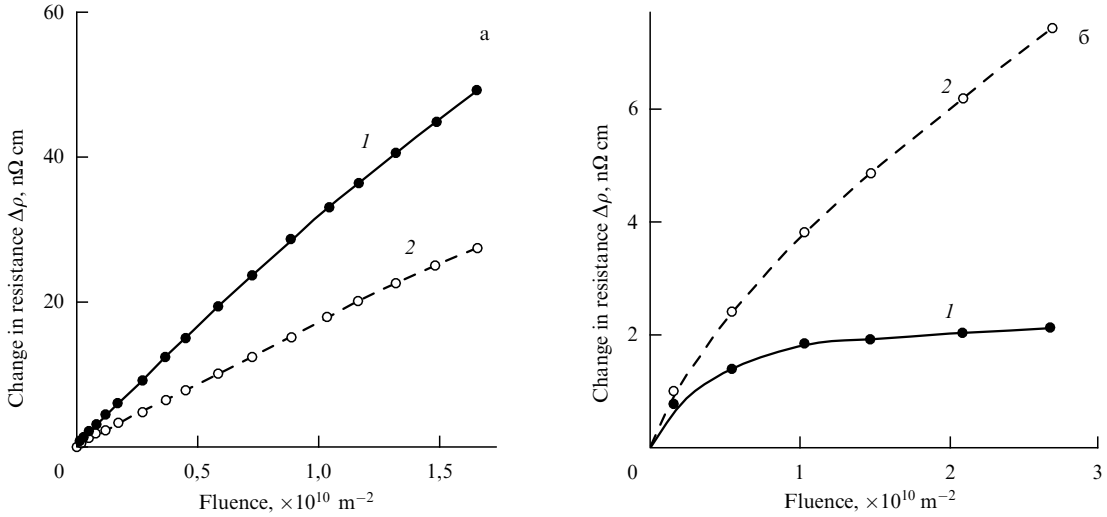

Figure 8. Effect of carbon ion fluence ($E = 60$ MeV) on electrical resistance in irradiated nanocrystalline (*1*) and macrocrystalline (*2*) gold samples at 15 K (a) and 300 K (b) (adapted from [101]).

each material has a specific optimal grain size ensuring resistance to amorphization and removal of radiation defects. These dependences are shown schematically in Fig. 9, where 5 energy bands are distinguished taking into account the sum of the free energies of grain boundaries and point defects, as well as the energy barrier for amorphization (transition from the crystalline state to the amorphous one). These bands can be described in terms of the processes proceeding in them as follows: (1) transition to the amorphous state without irradiation ($d < d_1$), e.g., as in silicon nanoparticles less than ~ 3 nm in size [106]; (2) transition to the amorphous state initiated by weak irradiation ($d_1 < d < d_2$); (3) the absence of radiation-induced amorphization in a grain size range $d_2 < d < d_3$; (4) irradiation leading to amorphization in a size range $d_3 < d < d_4$; (5) predominance of the free energy of defects in a size range $d_4 < d < d_{max}$ where boundaries play only a small role in their removal. Annihilation of defects by volume recombination prevails at $d > d_{max}$.

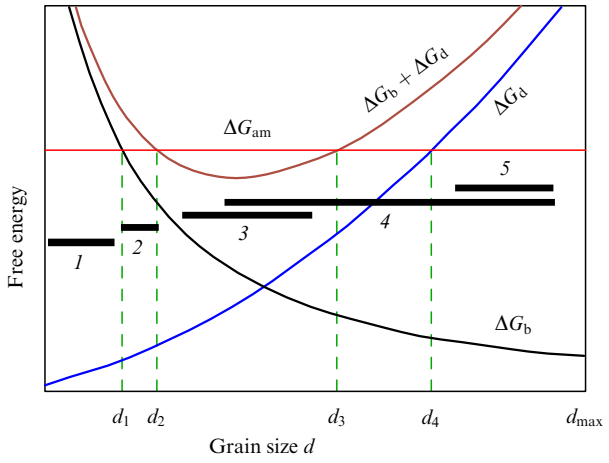

Figure 9. Effect of grain size on the free energies of grain boundaries ΔG_b, point defects ΔG_d, and their total value ($\Delta G_b + \Delta G_d$). ΔG_{am} is the amorphization energy barrier (adapted from [103]). See characteristics of energy bands (1–5) in the text.

The features of radiation-induced amorphization of nanocrystals embedded in an inert solid matrix were analyzed in [104]. It was shown that amorphization of a crystalline nanocluster in an inert matrix may be either accelerated (by proneness to radiation damage) or decelerated (due to radiation resistance). Realization of these options depends on the situation at the nanocluster–matrix interface, which can be (in contrast to macrocrystalline objects) either contracted (accelerated amorphization) or expanded (decelerated defect formation). These results qualitatively correspond to the data on the influence of the ion irradiation dose on the degree of amorphization of germanium nanocrystals in the SiO_2 matrix [91, 93].

The relationship between IVA recombination kinetics and size effects in radiation-induced amorphization was analyzed in [105]. It was shown that a reduction of the nanograin size can either increase or decrease radiation resistance, depending on the temperature that determines diffusion and defect recombination rates. An excess of vacancy defects remaining after predominant recombination of interstitial atoms at the grain boundaries creates prerequisites for amorphization. The authors of [105] undertook a detailed analysis of the temperature-dependent evolution of carbon and silicon atom defects in silicon carbide and arrived at the conclusion that nanocrystalline SiC is less resistant to radiation than its macrocrystalline counterpart. They attributed this difference to the presence of high-energy barriers for recombination of carbon IVA and 'interstitial hunger' leading to amorphization. However, taking into account planar packing defects of the SiC nanostructure in an MD, study [107] suggested a diametrically opposite conclusion confirmed by experiment (see Section 3.2).

It is frequently difficult to obtain and analyze exact information with the use of approaches employed in [102–105] due to a variety of interfering factors and assumptions; hence, the importance of the correct characteristic of interfaces (grain boundaries and junctions) and estimation of energy losses associated with irradiation of diatomic objects, such as oxides, carbides, nitrides, etc. [108–110]. Rutherford backscattering spectroscopy and secondary ion mass-spectrometry revealed the energy loss distribution in ion and electron subsystems during SiC irradiation with Au ions

in a wide energy range from ~ 70 keV to 15 MeV. This observation is of importance for the reliable estimation of the ion penetration depth and the interpretation of radiation effects [109].

It was shown by various methods that the effectiveness of grain boundaries as sinks for radiation defects (copper irradiation by He ions with an energy of 200 keV; fluence $(1-2)\times 10^{17}$ ions cm^{-2}; $T = 300-450\,^{\circ}$C) depends on boundary disorientation and orientation of crystallographic planes extending to the boundaries [110]. The maximum width of the defect-free region, i.e., the largest effective sink, near the $(\bar{1}03)//(14\bar{2}\bar{2}3)$ grain boundary was found at roughly a 45° disorientation; the sinks were smaller near $\Sigma 3(110)$ symmetric tilt boundaries even at greater disorientation angles.

3.2 Experimental results

Table 3 presents some of the most important results of an experimental study on the influence of radiation on the structure and properties of nanomaterials. As is known, the higher radiation resistance of ZrO_2 and Pd nanocrystalline samples irradiated with Kr ions compared with that of macrocrystalline objects was first reported in [111], which demonstrated the role of interfaces as sinks for radiation defects. The data in Table 3 confirm the results of [111] for other nanostructures, including metals, alloys, nanomaterials, oxides, and semiconductors. The findings for ferrite steels and tungsten [115, 116] provided a basis for the further development of research with a view to creating devices characterized by enhanced radiation resistance to be used in fusion–fission nuclear reactors of the new generation.

Also important are comparative experimental studies of macro- and nanocrystalline samples. Of special interest in this context are experiments on multilayer Cu/V and Cu/Nb films [8, 117]. These solid-state systems are immiscible.Variation of individual layer thickness without altering the total film thickness reveals the influence of the number of interfaces on the removal of radiation defects and changes in mechanical properties in response to irradiation. Figure 10 illustrates the effects of individual layer thickness in irradiated Cu/V films on He pore density, swelling, and hardness and its change [117]. These results indicate that a reduction in thickness h increases hardness but inhibits its changes in response to irradiation and decreases the number of He pores and swelling. Similar results were obtained in irradiation of other multilayer films, such as Cu/Nb, Fe/W, Al/Nb, etc. (see references in [8, 12, 120]).

The data in Table 3 on irradiation of 3C–SiC [114] are supplemented by the results of recent research concerning the influence of radiation on the structure and properties of nanocrystalline silicon carbide (see [107, 121–125]). This compound is remarkable in that it has a large number of polytypes and allows nanostructures to be obtained by various methods [126], which accounts for the difficulties encountered in the comparison of results of different authors. Ref. [122] shows that the behavior of nanostructured SiC

Table 3. Effects of ion irradiation in accelerators and neutron irradiation in reactors on nanomaterials (dpa — displacements per atom).

Object	Grain size, mn	Irradiation conditions				Result
		Particle	Energy, MeV	Temperature, K	Dose unit (dpa); fluence (ion cm^{-2}; n cm^{-2})	
Pd [111] ZrO_2 [111]	10 – 300 10 – 300	Kr Kr	4 0.24	293 293	3 – 8 dpa 210 dpa	Decrease in the number of radiation defects with reduction in grain size
$MgCa_2O_4$ [112]	4 – 12	Kr	0.3	100	12 – 96 dpa	Nanocrystals stable to amorphization
	$\sim 10^4$					Amorphization begins at 12 dpa
TiNi [113]	31 ± 6	Ar	1.5	293	0.2 – 5.6 dpa	No amorphization
	8×10^4					Amorphization begins at 0.4–2.5 dpa
3C – SiC [114]	36	Au	4	293	$10^{13} - 10^{15}$ ion cm^{-2}	Amorphization at 10^{14} ion cm^{-2}
	$\sim 10^3$					Amorphization at 10^{13} ion cm^{-2}
W – 0.3 % TiC [115]	50 –200	He	3	823	2×10^{19} ion cm^{-2}	Blistering at 2×10^{19} ion cm^{-2}
	Standard W					Blistering at 2×10^{18} ion cm^{-2}
W – 0.5 % TiC [115]	50 – 200	Neutrons	> 1	873	2×10^{20} n cm^{-2}	No radiation hardening
	Standard W					20% increase in hardening
Nanostructured ferrite steel 14 YWT [116]	~ 500 (grains) 2 – 5 (inclusions)	Neutrons	> 0.1	573 – 900	1.5 dpa	Insignificant radiation hardening and small decrease in ductility
Cu/V [117]	Layer thickness 1 – 200	He	0.05	293	6 dpa	Reduction in number of pores and radiation hardening with decreasing layer thickness
Cu [118]	Single crystal; $(20-30)\times 10^3$; ~ 15	He	0.2	723	2×10^{17} ion cm^{-2}	Minimal number of He pores in nanofilms
Fe – 0.1 % C [119]	$(44 \pm 0.8) \times 10^3$; 370 ± 60	Neutrons	> 1	328	1.15×10^{-3} dpa	Less changes in mechanical properties of nanosamples

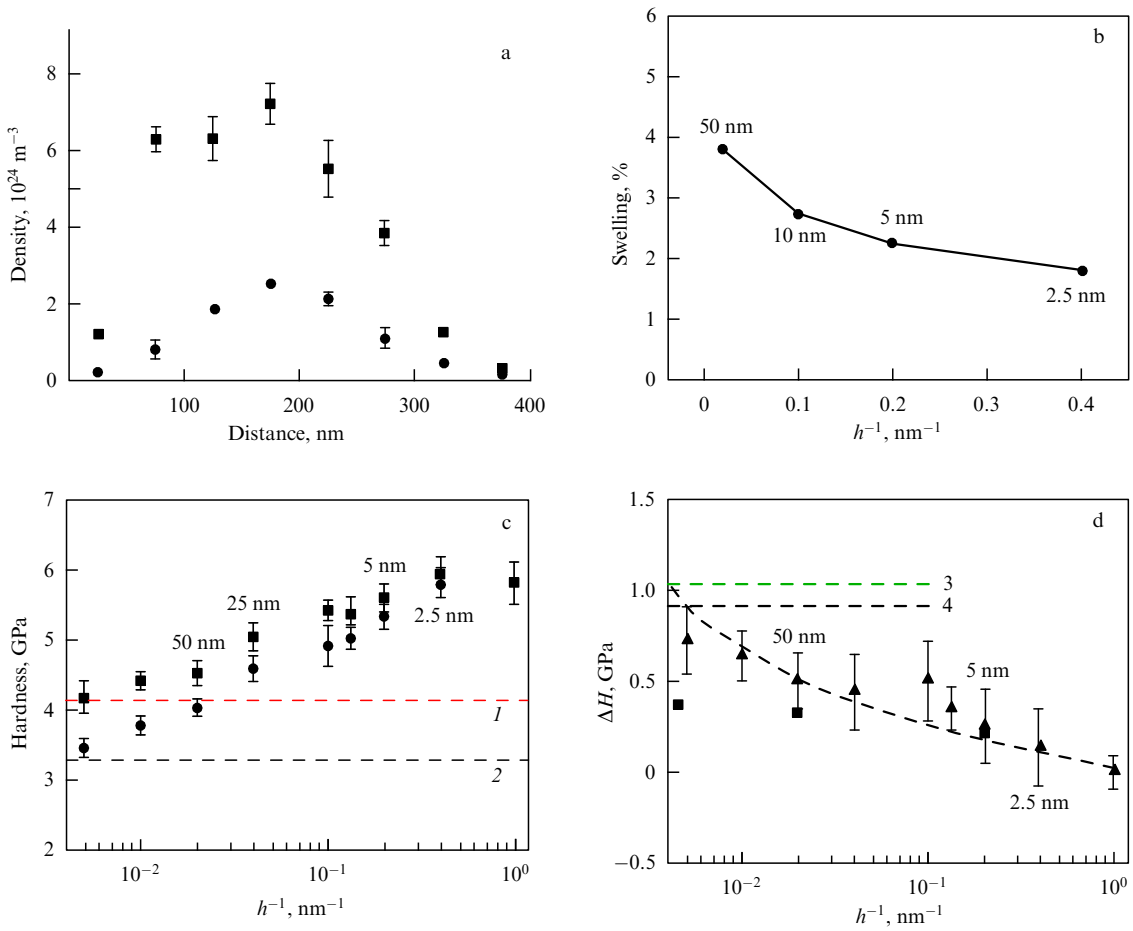

Figure 10. Changes in He pore density (a): ■ — Cu/V $h = 50$ nm, ● — Cu/V $h = 2.5$ nm; swelling (b); hardness (c): ■ is irradiated films, ● is intact films and radiation-induced hardness changes ΔH (d): with depth (a) and depending on individual layer thickness h (b, c, d) in multilayer Cu/V films irradiated with He ions ($E = 50$ keV, total fluence 6×10^{16} ion cm^{-2}). Figs c and d: *1* and *2* are hardness of irradiated and unaffected films estimated from additive considerations; *3* and *4* are hardness of 1 μm V and Cu films (adapted from [117]).

films irradiated by Au ions with an energy of 2 MeV ($T = 293$ K) is identical with the behavior of silicone carbide single crystals. Nevertheless, most researchers emphasize the enhanced radiation resistance of nanostructures of this compound. Interesting in this respect are the data on the influence of electron irradiation on the structure of SiC obtained by high-resolution *in situ* TEM [125]. The authors concluded that regeneration of radiation-induced defects (interstitial atoms and vacancies) occurs at (111) interfaces between planar defects (packing defects or twins), which promotes radiation resistance of nanostructured SiC.

The mechanisms of radiation defect formation and regeneration are being extensively investigated in other nanomaterials with a view to obtaining a deeper insight into their structural features. A study of the temperature dependence of nanohardness of three-layer Cu/Ni/Nb revealed much smaller changes in 5-nm-thick layers than in 10 nm and 30 nm ones [127]. A comparison of damages to multilayer Ag/Ni films inflicted by irradiation with He ions and protons showed that the former resulted in a much higher increase in hardening and its stronger dependence on the layer thickness (from 1 to 200 nm) than the latter [128]. Such a dependence was absent in proton irradiation, but high-resolution TEM demonstrated the formation of vacancy loops in Ag and interstitial loops in Ni that had a much weaker effect on radiation hardness than structural changes due to helium nanopore formation. Interactions of these nanopores and radiation defects with interfaces in multilayer films and plastically deformed layers are discussed in [129].

Grain growth in nanostructured metallic films (Au, Pt, Cu, Zr, and Zr-Fe) under the effect of irradiation with Ar ($E = 0.5$ MeV) and Kr ($E = 0.5-1$ MeV) ions was thoroughly investigated in a wide temperature range of 20–773 K [130] where three intervals can be distinguished, viz. purely thermal (strong temperature dependence of recrystallization), thermally-induced (joint temperature and radiation impact), and low-temperature (with weak thermal effect). The temperature of transition from the low-temperature interval to the combined one depended on the irradiated object, and its mean value at a homologous scale varied from $0.15T_m$ to $0.20T_m$. The theory of radiation-induced grain growth implies the formation of thermal peaks in cascades and subcascades and provides a basis for the description of such growth by an expression of type $L^n - L_0^n \sim K(Ft)$, where $n \sim 3$, F is the beam intensity (ion m^{-2} s^{-1}), t is the time, K is a constant depending on grain mobility and motive force, and L_0 is the initial grain size.

Comparison of radiation-induced segregations in irradiated coarse-grained and nanostructured ($d \sim 40$ nm) Cr–Ni 316 type steel in an atomic probe tomographic study showed that a redistribution of silicon, nickel, and chromium toward the grain boundaries and dislocations is less pro-

Table 4. Effect of radiation on the structure of nanocrystals in an amorphous matrix.

Object	Nanocrystal size, nm	Irradiation conditions				Result
		Ion	E, MeV	Dose unit (dpa)	Fluence (ion m^{-2})	
ZrO_2/SiO_2 [134] ZrO_2 [139]	~ 3	Xe	1	~ 0.8		Amorphization
	Single crystal	Xe	0.4	680		Crystalline state
Cu/SiO_2 [135, 136]	~ 2.5	Sn	5	0.16		Amorphization
	~ 8	Sn	5		10^{19}	Crystalline state
Au/SiO_2 [137]	3	Xe	1	~ 0.8		Crystalline state
	3 – 5	Sn	2.3		$10^{19} - 10^{20}$	Crystalline state
Ge/SiO_2 [91, 138]	4 – 8	Si	5		$10^{15} - 10^{19}$	Earlier amorphization of nanocrystals
Co/SiO_2 [92]	3.7 ± 1.0	Au	9		10^{17}	Amorphization

nounced [131], and homogeneous steel composition is better preserved in nanostructured samples than in coarse-grained ones. The influence of irradiation with Kr ions on the degradation behavior of $Cu_{1-x}M_x$ ($0.1 < x < 0.15$, M = Ag, Co, Fe, Mo, and Nb) film alloys, changes in their mutual solubility, nanoinclusion size, and matrix nanostructure were analyzed in [132]. The general problems pertaining to radiation processes in crystalline solid solutions based on metals and ionic compounds are considered regardless of nanostructure effects in monograph [133].

To conclude this section, we shall consider the influence of radiation on amorphization of nanostructures exemplified by crystalline nanoparticles of ZrO_2, Si, Cr, Co, Co, and Ge. Their irradiation in inert matrices like amorphous silicon oxide was shown to result in amorphization [91–93, 134–138]. Table 4 illustrates some of these results obtained with the use of nanocrystals implanted into ~ 2-μm-thick amorphous layers of SiO_2. The state and the composition of the nanocrystals were determined by several methods (high-resolution TEM, Rutherford backscattering spectroscopy, small-angle scattering, X-ray absorption spectroscopy, etc.) and the MD technique.

The most remarkable results in Table 4 pertain to amorphization of zirconium oxide, which usually escapes amorphization in the single crystalline state even at very high radiation doses [139], and to the irradiation of gold and copper nanocrystals (8 nm) resistant to amorphization. It was shown in [135–137] that the size factor (copper) and the nature of the nanocrystal (gold) have a marked effect on the radiation-induced nanocrystalline to amorphous state transition. A detailed study of irradiated nanocrystals of copper [136] helped to elucidate the role of Cu_2O formation during amorphization. A more detailed description of the behavior of nanoparticles and nanotubes based on BN, C, semiconductors, and metals (both free and bound inside inert matrices) following ion and electron irradiation can be found in [93], where data unlisted in Table 4 are additionally analyzed among other matters (e.g., irradiation of cobalt nanocrystals) and the necessity of further research is emphasized.

4. Behavior of nanomaterials under strain

The problem of achieving high energy densities and their influence on matter is comprehensively considered in monograph [1] by V E Fortov. Studies of nanomaterials in this respect are still scarce, and the available information largely pertains to fatigue resistance and partly to the effects of high static and dynamic pressure, behavior in strong magnetic fields, and related matters. Such information is of special importance as regards designing devices to generate strong and superstrong pulsed fields (over 60 T) in which the arising Lorentz forces create a pressure on the order of 1 GPa [2].

Polyfunctional materials in the form of Cu/Nb nanocomposites characterized by high conductivity (minimizing Ohmic losses) and strength (preventing degradation) that are used to make wire 2.5 mm in diameter (with a diameter of niobium fibers of ~ 140 nm) by hot extrusion and cold drawing have proved to be very suitable to manufacture solenoids generating ~ 70 T magnetic fields for work under cyclic conditions at cryogenic temperatures. As mentioned earlier [51–53], Cu/Nb nanocomposites have high strength and thermal stability. Methods for the further improvement of manufacturing technology and composition of Cu/Nb and Cu/Ag nanocomposite wires to be used in superstrong magnetic fields are described in [140, 141].

The peculiarities of structural relaxation and degradation of composite nanoparticles related to the generation of misfit dislocations in a core–shell system were considered by M Yu Gutkin in the framework of continuum mechanics [142].

The potential to considerably enhance nanomaterial strength (by reducing grain size and creating obstacles to dislocation shifts) necessitated the analysis of the fatigue characteristics (see [55, 143, 144]). Some recent studies have provided an insight into the mechanism of fatigue in nanomaterials. Figure 11 shows fatigue resistance curves for titanium, 08X18H10T stainless steel, and copper coarse-grained samples before and after strong plastic deformation by equal-channel angular pressing (ECAP) [145–147]. These data indicate that the advantage of nanostructured samples continues to remain in effect for a basic scope of fatigue tests (with the number of cycles N up to $10^6 - 10^7$) decreasing with growing N for copper and increasing for titanium. ECAP of steel samples gave rise to 100–250 nm structural elements, along with a large amount of deformation twins and lath martensite. Cyclic deformation was accompanied by dynamic twinning, recycling, recrystallization, and partial martensitic transformation [146]. Additional annealing after ECAP stimulated these processes and enhanced the fatigue resistance of nanostructured samples. Specifically, the fatigue

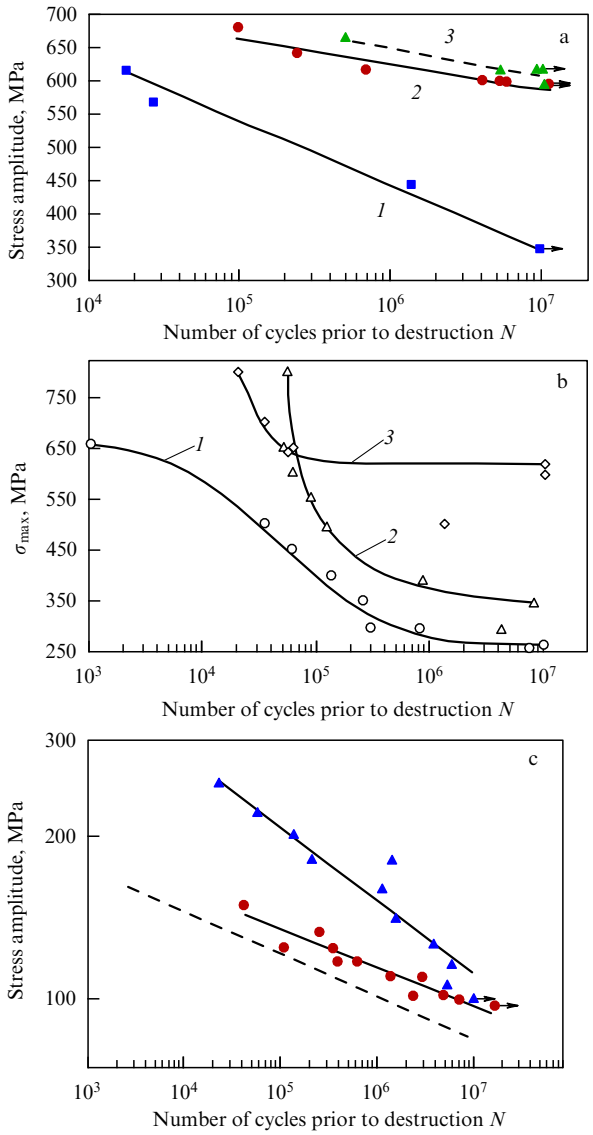

Figure 11. Fatigue resistance curves for titanium (a), 08X18H10T steel (b), and copper (c): (a) (*1*) coarse-grained samples, (*2*) post-ECAP samples, (*3*) post-ECAP/annealing (350 °C) samples; (b) (*1*) coarse-grained samples, (*2*) post-ECAP samples, (*3*) post-ECAP/annealing (550 °C) samples; (c) dashed line — coarse-grained samples, ● — cold-rolled samples, ▲ — post-ECAP samples (adapted from [145–147]), σ — stress (half-stress amplitude is plotted on the vertical axis in Fig. c).

strength of nanostructured copper samples in torsion tests was shown to be significantly higher than that of objects studied in tensile-and-compression tests, the discrepancy being due to the peculiarities of microcrack nucleation and propagation [147].

The ECAP of aluminum alloys not only enhanced their strength and plasticity but also somewhat improved the fatigue characteristics, even though the intricate nature of this phenomenon remains to be elucidated [148].

Importantly, ECAP increased resistance to corrosive cracking of an Zr–2.6% Nb alloy used in nuclear engineering [149]. Ultrafine-grained ($d = 200-700$ nm) samples of this material tested in a 1% iodine solution in methanol simulating the corrosive medium in the reactor zone (load $\sim 0.8\sigma_{0.2}$, $T = 20$ °C, $t = 50$ hr) exhibited a smaller diameter of corrosion pits and less pronounced changes in the mechanical properties than coarse-grained samples. Pit distribution in the former material was more uniform despite their greater number.

The results of Refs [145–149] defy an unambiguous interpretation. A comprehensive discussion of the influence of intensive plastic deformation on the physicomechanical properties of nanomaterials can be found in Ref. [150], where the dual role of grain boundaries is emphasized in the context of a fatigue problem: on the one hand, they contribute to the enhancement of strength and endurance limit, but they initiate crack nucleation, on the other hand. Investigations into the mechanisms behind crack nucleation and propagation in nanomaterials after ECAP are just beginning. A study of twin boundaries in copper and its alloys showed that crack formation in low-cycle fatigue depends on the packing defect energy, the character of the glide planes, and the crystallographic orientation of the matrix and twin boundaries [151]. Modeling resistance to fatigue crack growth in nanomaterials by MD and damage mechanics methods was undertaken in [152]. It was shown that crack growth can be slowed by decreasing the twin thickness and the intertwin distance within an area of less than 20 nm.

An explanation of the influence of intensive plastic deformation (or megaplastic deformation in the terminology of [153]) on the behavior of nanomaterials depends on the level of understanding of the nature of structural and phase transformations in these conditions. This problem is a matter of lively discussions [159, 153, 154]) but lies beyond the scope of the present review.

High pressure has long been used to consolidate nanoparticles in refractory compounds (carbides, nitrides, borides) and diamond to manufacture bulk nanostructured samples [31, 155, 156]. The behavior of nanomaterials at high static and dynamic pressure was studied in order to follow up the evolution of their phase composition. In 8–20 nm TiO_2 particles, strong shock compression (10–45 GPa, $T = 500-2500$ K) induced the phase transformation of a tetragonal modification (anatase, $P4/mnm$ structure group) into an orthorhombic one (columbite, $Pbcn$ structure group). A further increase in pressure and temperature gave rise to tetragonal rutile microstructures ($I4_1/amd$ structure group) [157, 158]. Graphite-like carbon nitride C_3N_4 exposed in a diamond anvil cell to a pressure of 30 GPa at 1600 K transformed into the orthorhombic phase, which remained stable at pressures of up to 125 GPa and a temperature of 3000 K [159]. The resulting phase is supposed to have formula C_2N_2X, where $X = NH, CH_2$. However, attempts to synthesize by this method a cubic C_3N_4 with potentially high mechanical properties have thus far failed.

5. Conclusion

The present review covers a by far incomplete list of nanoobjects that does not include semiconductors and many other functional materials, polymer and hybrid compositions, nanoelectromechanical units, or nanobiomaterials, to say nothing about nanoglasses [160], not because these issues lie outside the scope of the author's interest but because of a lack of relevant systematic stability information.

Nevertheless, the data cited provide many examples of the application of metallic nanomaterials under extreme temperature, radiation, and deformation conditions. In this context, recently proposed methods for the evaluation of the thermal stability of nanomaterials [26–28] appear to be very promising for practical applications. They create prerequi-

sites for the extensive use of nanomaterials in new, rapidly developing technologies. At the same time, many aspects related to long-term stability, prevention of anomalous grain growth, the choice of optimal starting nanostructures, etc. await additional experimental and theoretical studies to be elucidated. Equally important are investigations of the joint actions of various extreme factors whose synergistic effects may aggravate the risk of damage and imply the necessity of a deeper understanding and theoretical description of the phenomena of interest.

The author thanks V V and C V Klyucharev for the assistance in the preparation of this review. The work was supported by the Russian Foundation for Basic Research (grant No. 13-03-01014) and the Department of Chemistry and Material Sciences, Russian Academy of Sciences (program No. 8).

References

1. Fortov V E *Ekstremal'nye Sostoyania Veshchestva* (Extreme States of Matter) (Moscow: Fizmatlit, 2010)
2. Misra A, Thilly L *MRS Bull.* **35** 965 (2010)
3. Fortov V E, Mintsev V B *Russ. Chem. Rev.* **82** 597 (2013); *Usp. Khim.* **82** 597 (2013)
4. Bourne N *Materials in Mechanical Extremes. Fundamentals and Applications* (Cambridge: Cambridge Univ. Press, 2013)
5. Low I M, Sakka Y, Hu C F (Eds) *MAX Phases and Ultra-High Temperature Ceramics for Extreme Environments* (Hershey, PA: IGI Global, 2013)
6. Bertolus M et al. (Eds) *Advanced Materials in Extreme Environments* (Mater. Res. Soc. Symp. Proc., Vol. 1645) (Warrendale: MRS, 2014)
7. Andrievski R A *Kompozity Nanostrukt*. (4) 35 (2009)
8. Demkowicz M J, Bellon P, Wirth B D *MRS Bull.* **35** 992 (2010)
9. Boldyreva E V *Herald Russ. Acad. Sci.* **82** 423 (2012); *Vest. Ross. Akad. Nauk* **82** 982 (2012)
10. Andrievskii R A *Protect. Met. Phys. Chem. Surf.* **49** 528 (2013); *Fizikokhim. Poverkh. Zashchita Mater.* **49** 491 (2013)
11. Andrievski R A *Osnovy Nanostrukturnogo Materialovedeniya. Vozmozhnosti i Problemy* (Fundamentals of Nanostructured Materials Science. Potentials and Problems) (Moscow: BINOM. Laboratoriya Znanii, 2012)
12. Andrievskii R A *Nanotechnol. Russ.* **6** 357 (2011); *Ross. Nanotekhnol.* **6** (5–6) 34 (2011)
13. Andrievski R A *Rev. Adv. Mater. Sci.* **29** 54 (2011)
14. Andrievski R A *J. Mater. Sci.* **49** 1449 (2014)
15. Andrievski R A *Russ. Chem. Rev.* **83** 365 (2014); *Usp. Khim.* **83** 365 (2014)
16. Ovid'ko I A *Fiz. Mekh. Mater.* **8** 174 (2009)
17. Upmanyu M et al. *Acta Mater.* **54** 1707 (2006)
18. Bernstein N *Acta Mater.* **56** 1106 (2008)
19. Chaim R *Scr. Mater.* **66** 269 (2012)
20. Zizak I *Nucl. Instrum. Meth. Phys. Res. B* **267** 944 (2009)
21. Novikov V Yu *Acta Mater.* **58** 3326 (2010)
22. Novikov V Yu *Mater. Lett.* **68** 413 (2012)
23. Klinger L et al. *J. Mater. Sci.* **43** 5068 (2008)
24. Trelewicz J R, Schuh Ch A *Phys. Rev. B* **79** 094112 (2009)
25. Chookajorn T, Mordoch H A, Schuh Ch A *Science* **337** 951 (2012)
26. Murdoch H, Schuh Ch A *Acta Mater.* **61** 2121 (2013)
27. Saber M et al. *J. Appl. Phys.* **113** 063515 (2013)
28. Darling K A et al. *Comput. Mater. Sci.* **84** 255 (2014)
29. Hu W et al. *J. Appl. Phys.* **105** 104310 (2009)
30. Hu W, Song X, Zhang Z *Appl. Phys. Lett.* **97** 181911 (2010)
31. Andrievski R A, Ragulya A V *Nanostrukturnye Materialy* (Nanostructured Materials) (Moscow: Akademiya, 2005)
32. Hu W et al. *Nanoscale* **1** 238 (2009)
33. Hu W W, Song X Y, Zhang Z X *NANO Brief Rep. Rev.* **7** 125012 (2012)
34. Zhang R F, Veprek S *Thin Solid Films* **516** 2264 (2008)
35. Sheng S H, Veprek S *Acta Mater.* **59** 297 (2011)
36. Sheng S H, Zhang R F, Veprek S *Acta Mater.* **59** 3498 (2011)
37. Ivashchenko V I et al. *Phys. Rev. B* **85** 195403 (2012)
38. Ivashchenko V I et al. *Phys. Rev. B* **86** 014110 (2012)
39. Ivashchenko V I, Veprek S *Thin Solid Films* **545** 391 (2013)
40. Darling K A et al. *Mater. Sci. Eng. A* **528** 4365 (2011)
41. Atwater M A, Scattergood R O, Koch C C *Mater. Sci. Eng. A* **559** 250 (2013)
42. Koch C C et al. *J. Mater. Res.* **28** 1785 (2013)
43. Atwater M A et al. *Mater. Sci. Eng. A* **558** 226 (2012)
44. Darling K A et al. *J. Alloys Comp.* **573** 142 (2013)
45. Frolov T et al. *Acta Mater.* **60** 2158 (2012)
46. Özerinç S et al. *Scr. Mater.* **67** 720 (2012)
47. Koch C C et al. *Mater. Sci. Forum* **715–716** 323 (2012)
48. Darling K A et al. *J. Mater. Res.* **28** 1813 (2013)
49. Wang X L et al. *J. Alloys Comp.* **529** 96 (2012)
50. Anderoglu O et al. *J. Appl. Phys.* **103** 094322 (2008)
51. Karpov M I et al. *Materialovedenie* **2** 47 (2004)
52. Karpov M I et al. *Deform. Razrushenie Mater.* (11) 2 (2007)
53. Zheng Sh et al. *Nature Commun.* **4** 1696 (2013)
54. Liu X C, Zhang H W, Lu K *Science* **342** 337 (2013)
55. Andrievski R A, Glezer A M *Phys. Usp.* **52** 315 (2009); *Usp. Fiz. Nauk* **179** 337 (2009)
56. Arpin K A et al. *Nature Commun.* **4** 2530 (2013)
57. Ma Z, Dai S *Nano Res.* **4** 3 (2011)
58. Prieto G et al. *Nature Mater.* **12** 34 (2013)
59. Gupta A et al. *Mater. Sci. Forum* **653** 87 (2010)
60. Castro R H R *Mater. Lett.* **96** 45 (2013)
61. Chokshi A H *Scr. Mater.* **59** 726 (2008)
62. Gorelik S S, Dobatkin S V, Kaputkina L M *Rekristallizatsiya Metallov i Splavov* (Recrytstallization of Metals and Alloys) (Moscow: MISIS, 2005)
63. Cheng L, Hibbard G D *Mater. Sci. Eng. A* **492** 128 (2008)
64. Ames M et al. *Acta Mater.* **56** 4255 (2008)
65. Gottstein G, Shvindlerman L S, Zhao B *Scr. Mater.* **62** 914 (2010)
66. Konkova T et al. *Scr. Mater.* **63** 921 (2010)
67. Hattar K et al. *Acta Mater.* **56** 794 (2008)
68. Kacher J et al. *Mater. Sci. Eng. A* **528** 1628 (2011)
69. Paul H, Krill C E *Scr. Mater.* **65** 5 (2011)
70. Kotan H et al. *J. Mater. Sci.* **48** 2251 (2013)
71. Koch C C et al. *Structural Nanocrystalline Materials: Fundamentals and Applications* (Cambridge: Cambridge Univ. Press, 2007); Translated into Russian: *Konstruktsionnye Nanokristallicheskie Materialy. Nauchnye Osnovy i Prilozheniya* (Moscow: Fizmatlit, 2012)
72. Mannesson K et al. *Acta Mater.* **59** 1912 (2011)
73. McKie A et al. *Int. J. Refr. Met. Hard Mater.* **41** 66 (2013)
74. Novikov V Yu *Mater. Lett.* **65** 2618 (2011)
75. Novikov V Yu *Int. J. Mat. Res.* (4) 446 (2011)
76. Novikov V Yu *Mater. Lett.* **84** 136 (2012)
77. Novikov V Yu *Mater. Lett.* **100** 271 (2013)
78. Trushin Yu V *Radiatsionnye Protsessy v Mnogokomponentnykh Materialakh* (Radiation Processes in Multicomponent Materials) (St. Petersburg: FTI im. A.F. Ioffe, 2002)
79. Wurster S, Pippan R *Scr. Mater.* **60** 1083 (2009)
80. Andrievskii R A *Phys. Met. Metallogr.* **110** 229 (2010); *Fiz. Met. Metalloved.* **110** 243 (2010)
81. Samaras M et al. *Phys. Rev. Lett.* **88** 125505 (2002)
82. Voegeli W, Albe K, Hahn H *Nucl. Instrum. Meth. Phys. Res. B* **202** 230 (2003)
83. Samaras M et al. *J. Nucl. Mater.* **323** 213 (2003)
84. Mayr S G, Averback R S *Phys. Rev. B* **68** 075419 (2003)
85. Mayr S G, Ashkenazy Y, Averback R S *Nucl. Instrum. Meth. Phys. Res. B* **212** 246 (2003)
86. Samaras M et al. *J. Nucl. Mater.* **351** 47 (2006)
87. Millett P C et al. *Appl. Phys. Lett.* **93** 261902 (2008)
88. Morishita K et al. *J. Nucl. Mater.* **386–388** 30 (2009)
89. Millet P C et al. *Int. J. Mater. Res.* **100** 550 (2009)
90. Psakhie S G et al. *Crystallogr. Rep.* **54** 1002 (2009); *Kristallogr.* **54** 1053 (2009)
91. Djurabekova F et al. *Nucl. Instrum. Meth. Phys. Res. B* **267** 1235 (2009)
92. Sprouster D J et al. *Phys. Rev. B* **81** 155414 (2010)
93. Krasheninnikov A V, Nordlund K *Appl. Phys. Rev.* **107** 071301 (2010)
94. Bai X-M et al. *Science* **327** 1631 (2010)

95. Yang Y, Huang H, Zinkle S J *J. Nucl. Mater.* **405** 261 (2010)
96. Swaminathan N et al. *Acta Mater.* **58** 2843 (2010)
97. Åhlgren E H et al. *Appl. Phys. Lett.* **100** 233108 (2012)
98. Katoh Y et al. *Curr. Opin. Solid State Mater. Sci.* **16** 143 (2012)
99. Bai X-M et al. *Phil. Mag.* **92** 1469 (2012)
100. Voronina E N, Novikov L S *Bull. Russ. Acad. Sci. Phys.* **77** 814 (2013); *Izv. Ross. Akad. Nauk Fiz.* **77** 897 (2013)
101. Chimi Y et al. *J. Nucl. Mater.* **297** 355 (2001)
102. Ovid'ko I A, Sheinerman A G *Appl. Phys. A* **81** 1083 (2005)
103. Shen T D *Nucl. Instrum. Meth. Phys. Res. B* **266** 921 (2008)
104. Oksengendler B L et al. *JETP* **111** 415 (2010); *Zh. Eksp. Teor. Fiz.* **138** 469 (2010)
105. Swaminathan N, Morgan D, Szlufarska I *Phys. Rev. B* **86** 214110 (2012)
106. Shen T D et al. *J. Mater. Res.* **10** 139 (1995)
107. Zhang Y et al. *Phys. Chem. Chem. Phys.* **14** 13429 (2012)
108. Thomé L et al. *Nucl. Instrum. Meth. Phys. Res. B* **307** 43 (2013)
109. Jin K et al. *Nucl. Instrum. Meth. Phys. Res. B* **307** 65 (2013)
110. Han W et al. *Acta Mater.* **60** 6341 (2012)
111. Rose M, Balogh A G, Hahn H *Nucl. Instrum. Meth. Phys. Res. B* **127–128** 119 (1997)
112. Shen T D et al. *Appl. Phys. Lett.* **90** 263115 (2007)
113. Kilmametov A R et al. *Scr. Mater.* **59** 1027 (2008)
114. Leconte Y et al. *MRS Symp. Proc.* **981** JJ07 (2007)
115. Kurushita H et al. *J. Nucl. Mater.* **377** 34 (2008)
116. McClintock D A et al. *J. Nucl. Mater.* **386–388** 307 (2009)
117. Fu E G et al. *J. Nucl. Mater.* **407** 178 (2010)
118. Han W et al. *J. Mater. Res.* **28** 2763 (2013)
119. Alsabbagh A, Valiev R Z, Murty K L *J. Nucl. Mater.* **443** 302 (2013)
120. Demkowicz M J, Misra A, Caro A *Curr. Opin. Solid State Mater. Sci.* **16** 101 (2012)
121. Semenov A V *Semiconductors* **43** 1322 (2009); *Fiz. Tekh. Poluprovodn.* **43** 1362 (2009)
122. Jiang W et al. *Phys. Rev. B* **80** 161301(R) (2009)
123. Katoh Y et al. *J. Nucl. Mater.* **417** 400 (2011)
124. Gosset D et al. *Prog. Nucl. Energy* **37** 52 (2012)
125. Ishimaru M et al. *Appl. Phys. Lett.* **103** 033104 (2013)
126. Andrievski R A *Russ. Chem. Rev.* **78** 821 (2009); *Usp. Khim.* **78** 899 (2009)
127. Schoepner R et al. *MRS Symp. Proc.* **1645** ZZ4.04 (2014)
128. Yu K et al. *J. Nucl. Mater.* **440** 310 (2013)
129. Beyerlein I J et al. *Mater. Today* **16** 443 (2013)
130. Kaomi L et al. *J. Appl. Phys.* **104** 073525 (2008)
131. Etienne A et al. *Ultramicroscopy* **111** 659 (2011)
132. Chee S W et al. *Acta Mater.* **58** 4088 (2010)
133. Gladyshev G *Radiation Processes in Crystal Solid Solutions* (Bussum: Bentham e-Books, 2012)
134. Meldrum A, Boatner L A, Ewing R C *Phys. Rev. Lett.* **88** 025503 (2001)
135. Johannessen B et al. *Appl. Phys. Lett.* **90** 073119 (2007)
136. Johannessen B et al. *Phys. Rev. B* **76** 184203 (2007)
137. Kluth P et al. *Phys. Rev. B* **74** 014202 (2006)
138. Ridgway M C et al. *Phys. Rev. B* **71** 094107 (2005)
139. Sickafus K E et al. *J. Nucl. Mater.* **274** 66 (1999)
140. Han K et al. *MRS Symp. Proc.* **1645** ZZ7.03 (2014)
141. Thilly L et al. *MRS Symp. Proc.* **1645** ZZ7.04 (2014)
142. Gutkin M Yu *Nanomater. Energy* **2** 193 (2013)
143. Valiev R Z, Aleksandrov I V *Ob'emnye Nanostrukturnye Metallicheskie Materialy: Poluchenie, Struktura i Svoistva* (Bulk Nanostructured Metallic Materials: Fabrication, Structure and Properties) (Moscow: Akademkniga, 2007)
144. Zehetbauer M J, Zhu Y T (Eds) *Bulk Nanostructured Materials* (Weinheim: Wiley-VCH Verlag CmbH, 2009)
145. Semenova I P et al. *Mater. Sci. Eng. A* **503** 92 (2009)
146. Dobatkin S V et al. *Russ. Metall.* **11** 954 (2012); *Metally* (6) 45 (2012)
147. Li R H et al. *Acta Mater.* **61** 5857 (2013)
148. Sabirov I, Murashkin M Yu, Valiev R Z *Mater. Sci. Eng. A* **560** 1 (2013)
149. Nikulin S A et al. *Metal Sci. Heat Treatm.* **54** (7–8) 407 (2012); *Metalloved. Term. Obrab. Met.* (8) 32 (2012)
150. Estrin A, Vinogradov A *Acta Mater.* **61** 782 (2013)
151. Zhang P et al. *Scr. Mater.* **66** 854 (2012)
152. Chowdhury P B et al. *Acta Mater.* **61** 2531 (2013)
153. Glezer A M *Phys. Usp.* **55** 522 (2012); *Usp. Fiz. Nauk* **182** 559 (2012)
154. Teitel E I et al. *Phys. Met. Metallogr.* **13** 1162 (2012); *Fiz. Met. Metalloved.* **113** 1230 (2012)
155. Andrievski R A *Russ. Chem. Rev.* **74** 1061 (2005); *Usp. Khim.* **74** 1163 (2005)
156. Sumiya H, Irifune T *J. Mater. Res.* **22** 2345 (2007)
157. Shul'ga Yu M et al. *Tech. Phys. Lett.* **36** 841 (2010); *Pis'ma Zh. Tekh. Fiz.* **36** (18) 26 (2010)
158. Molodets A M, Golyshev A A, Shul'ga Yu M *Tech. Phys.* **58** 1029 (2013); *Zh. Tekh. Fiz.* **83** (7) 100 (2013)
159. Kojima Y, Ohfuji H *Diamond Related Mater.* **39** 1 (2013)
160. Andrievski R A *Phys. Usp.* **56** 261 (2013); *Usp. Fiz. Nauk* **183** 277 (2013)